Supporting Information for

"Catalytic Activity Trends of Pyrite Transition Metal Dichalcogenides for Oxygen Reduction and Evolution"

Wooseok Lee[a], Jongseung Kim[a], Heejin Kim[b], and Seoin Back[a],**

[a] Department of Chemical and Biomolecular Engineering, Institute of Emergent Materials, Sogang University, Seoul 04107, Republic of Korea

[b] Division of Analytical Science, Korea Basic Science Institute (KBSI), Yuseong-gu, Daejon 34133, Republic of Korea

Supplementary Note : *U–J (U$_{eff}$)* Values for TMDs

To determine appropriate *U−J* values for calculating ORR/OER catalytic activity of pyrite TMDs systems, four strategies were considered as listed below.

1. *U−J (U$_{eff}$)* values from previous literature

Most frequently, U−J values (or U$_{eff}$) were taken from the previous literature, where the previous literature calculated those values by fitting experimental values of by using a linear response approach, which will be discussed in the following. A summary of various U−J values used for pyrite TMDs and the corresponding references are in **Table S4** and **Table S5**. As indicated in **Table S4** and **Table S5**, there is no consensus in U−J values for pyrite TMDs even though same functional was used.

2. *U−J (U$_{eff}$)* values from Materials Project

The largest database of inorganic materials, The Materials Project[1], determined U−J values by fitting experimental formation enthalpies. We note that U-correction was only applied for oxide materials and all TMDs were treated by PBE in the Materials Project database. Since not all experimental formation enthalpies of TMDs are available, thus this strategy is not applicable for TMDs.

3. *U−J (U$_{eff}$)* values from experimental results

When experimental photoelectron spectroscopy (PES) or bandgap values are available, U−J values that most closely reproduce experimental values were chosen[2]. For TMDs considered in this work, bandgap values of only five out of twelve TMDs have been reported and Co-based TMDs are known to be metallic, thus this approach is not applicable either.

4. *U−J (U$_{eff}$)* values from linear response method

Linear response method proposed by Cococcioni and Gironcoli[3] is conventionally used for its good reproducibility of experimental results. In this approach, the effective U parameters (U$_{eff}$) are calculated from the difference between the inverse bare (non-interacting) density response, χ_0^{-1}, and the inverse self-consistent (interacting) density response, χ^{-1}. We split metal atoms into two groups (atom 1, and atom 2-32) and included small perturbations (± 0.08, ± 0.05, ± 0.02 eV) to atom 1 with 2×2×2 supercell consisting of 96 atoms (containing 32 metal atoms and 64 chalcogen atoms) to avoid errors induced by interactions between perturbations and their periodic images. Using the determined U$_{eff}$ values, we performed bulk optimizations and compared the lattice parameters with experimental results (**Table S6**). Notably, the percent difference

in the lattice parameters was found to be significant, especially for Fe and Co based TMDs.

As discussed above, several approaches were either unavailable due to the lack of experimental data or incapable of reproducing experimental values.

Surface catalytic processes are significantly affected by geometric and electronic properties[4]. For the former, since the surface catalytic processes are accompanied by the adsorption, cleavage and association of reactant molecules, the geometric parameters of active sites can alter the binding geometry and energy, thus impacting the catalytic activity prediction. In this point of view, the validity of the lattice parameter is essential for estimating the activity of materials.

Thus, we fitted U_{eff} with respect to the experimental lattice parameters. Although this approach is not perfect either, it reproduced some of experimental catalytic results for TMDs. For example, our computational method predicted $CoSe_2$ and $CoTe_2$ to be active for OER in agreement with the experimental literature[5, 6].
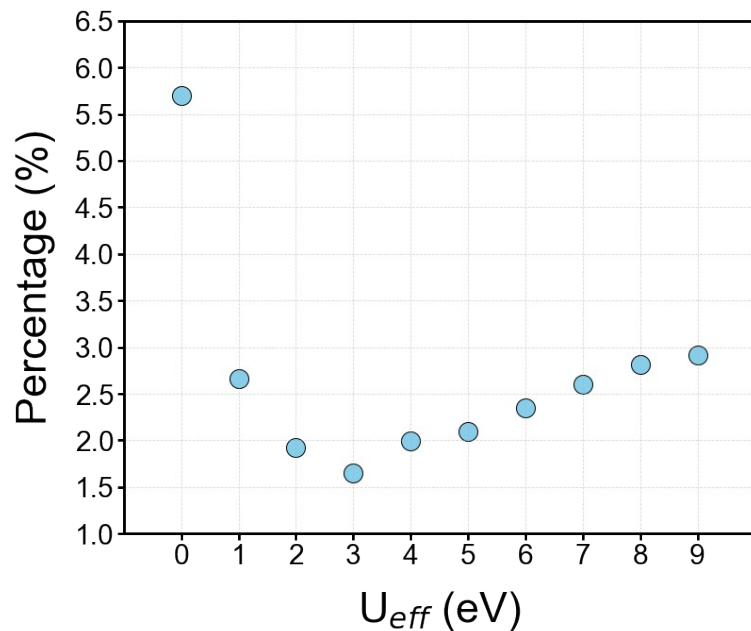
Figure S1. The percentage value of the average difference between experimentally measured and DFT calculated lattice parameters of Mn-based TMDs (MnS_2, $MnSe_2$ and $MnTe_2$) with varying U_{eff} values.

a   b
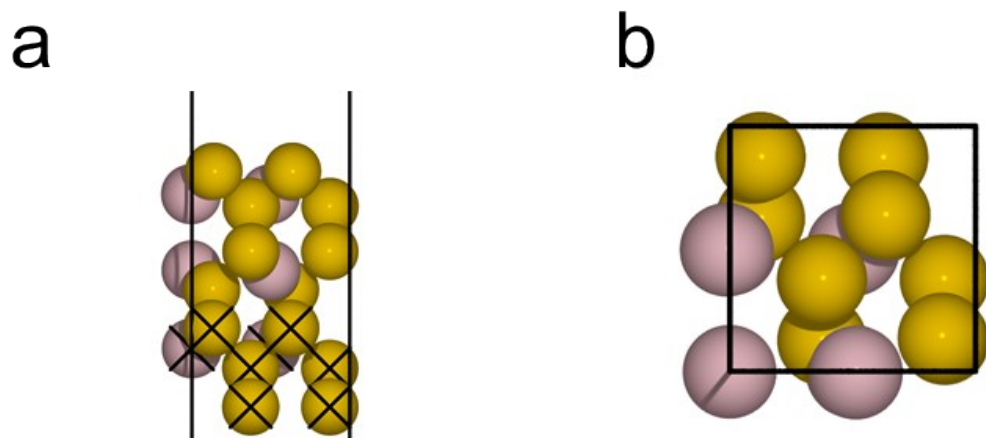
Figure S2. (a) Side and (b) top view of (001) TMD surface structures. Color codes: pink (metal) and yellow (chalcogen). Marked atoms were fixed during the geometry optimization.
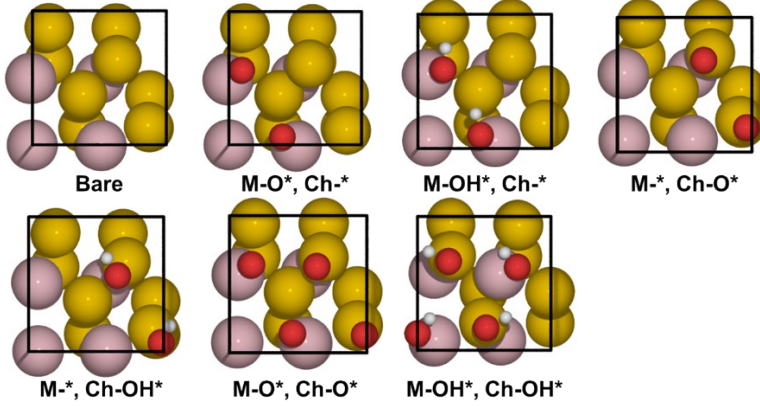
Figure S3. Seven different surface coverages considered to construct the surface Pourbaix diagrams, where M indicates metal sites (Mn, Fe, Co, Ni) and Ch indicates chalcogen sites (S, Se, Te).
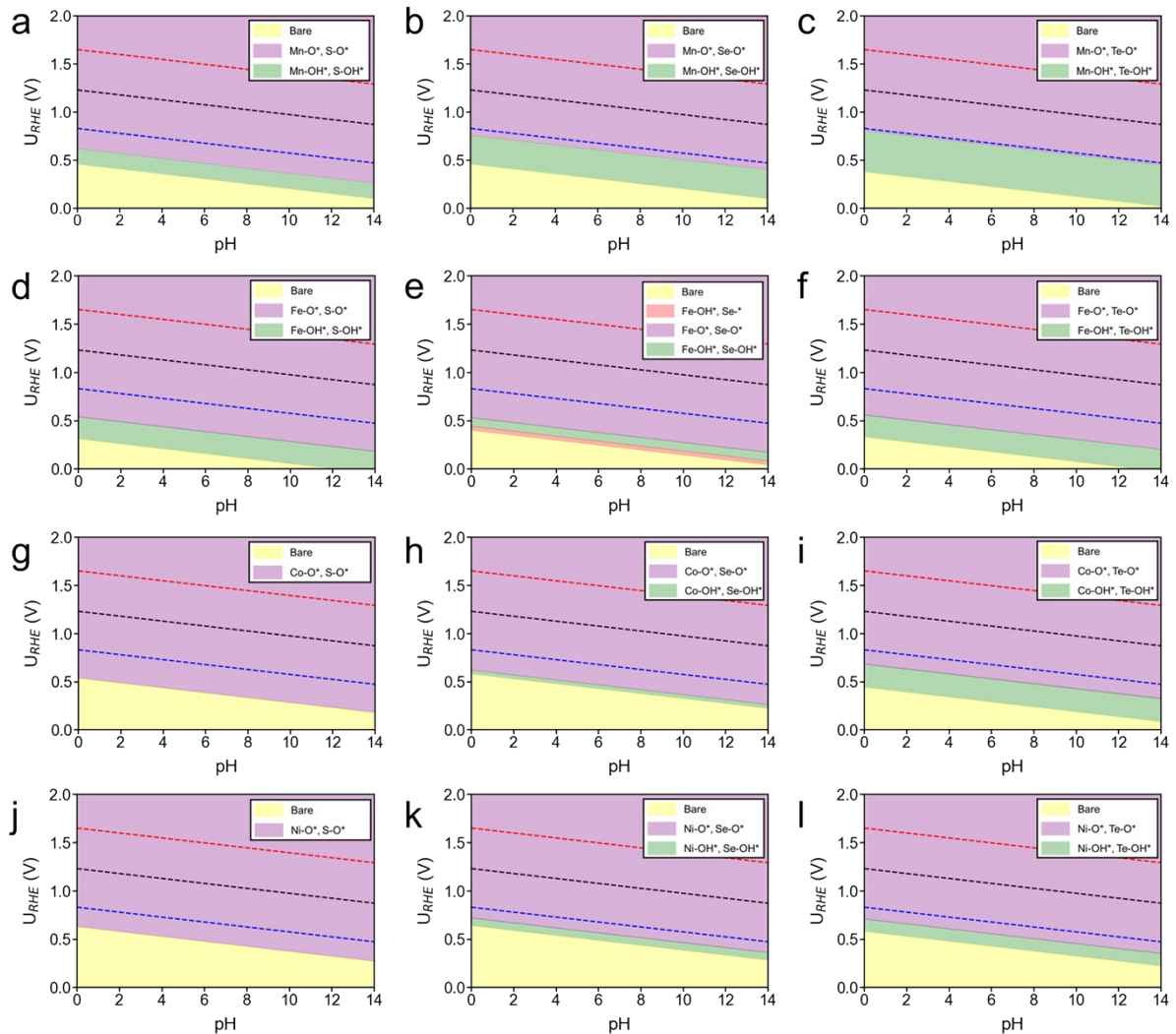

Figure S4. The surface Pourbaix diagrams for (001) surface of all TMDs. (a) MnS$_2$, (b) MnSe$_2$, (c) MnTe$_2$, (d) FeS$_2$ (e) FeSe$_2$ (f) FeTe$_2$ (g) CoS$_2$ (h) CoSe$_2$ (i) CoTe$_2$ (j) NiS$_2$ (k) NiSe$_2$ and (l) NiTe$_2$. In all cases, O*-covered (M-O*/Ch-O*, purple) surfaces are found to be

most stable under both ORR (blue dashed line) and OER (red dashed line) operating conditions. Black dashed line indicates the equilibrium potential of ORR/OER.
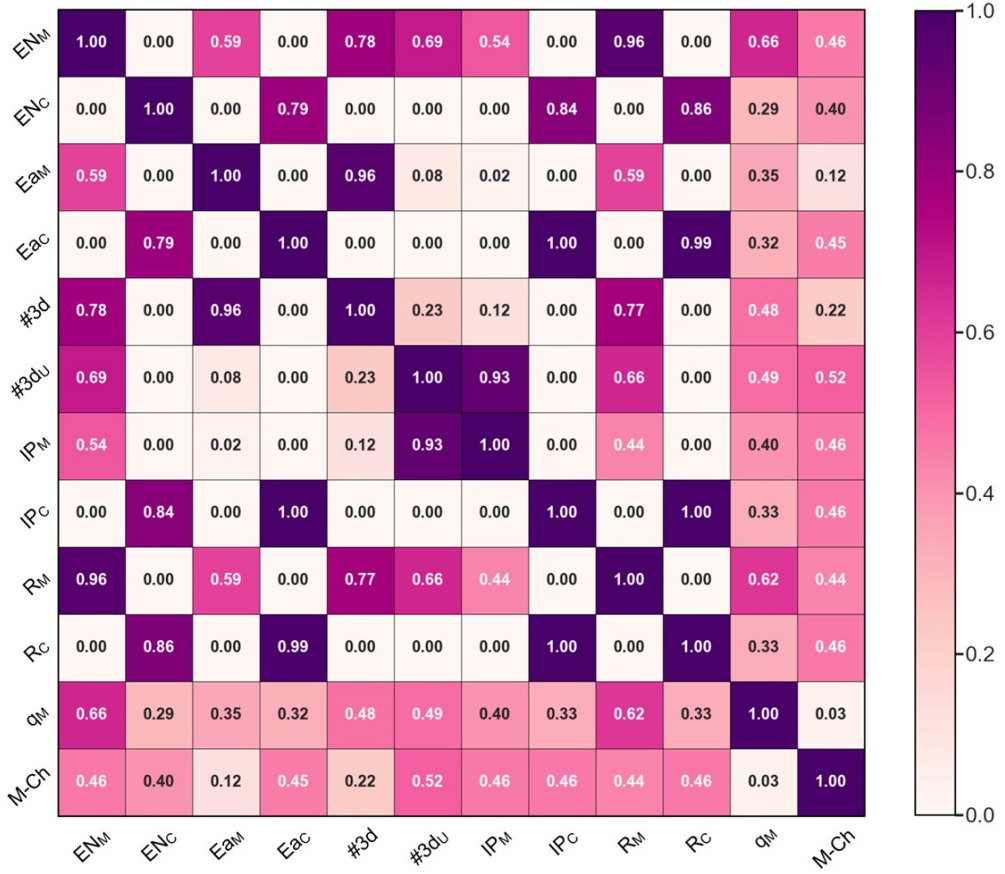
Figure S5. Pearson correlation coefficient matrix of all features considered in this work. The color bar represents correlation coefficients between two features. Explanations of features can be found in **Table S3**.
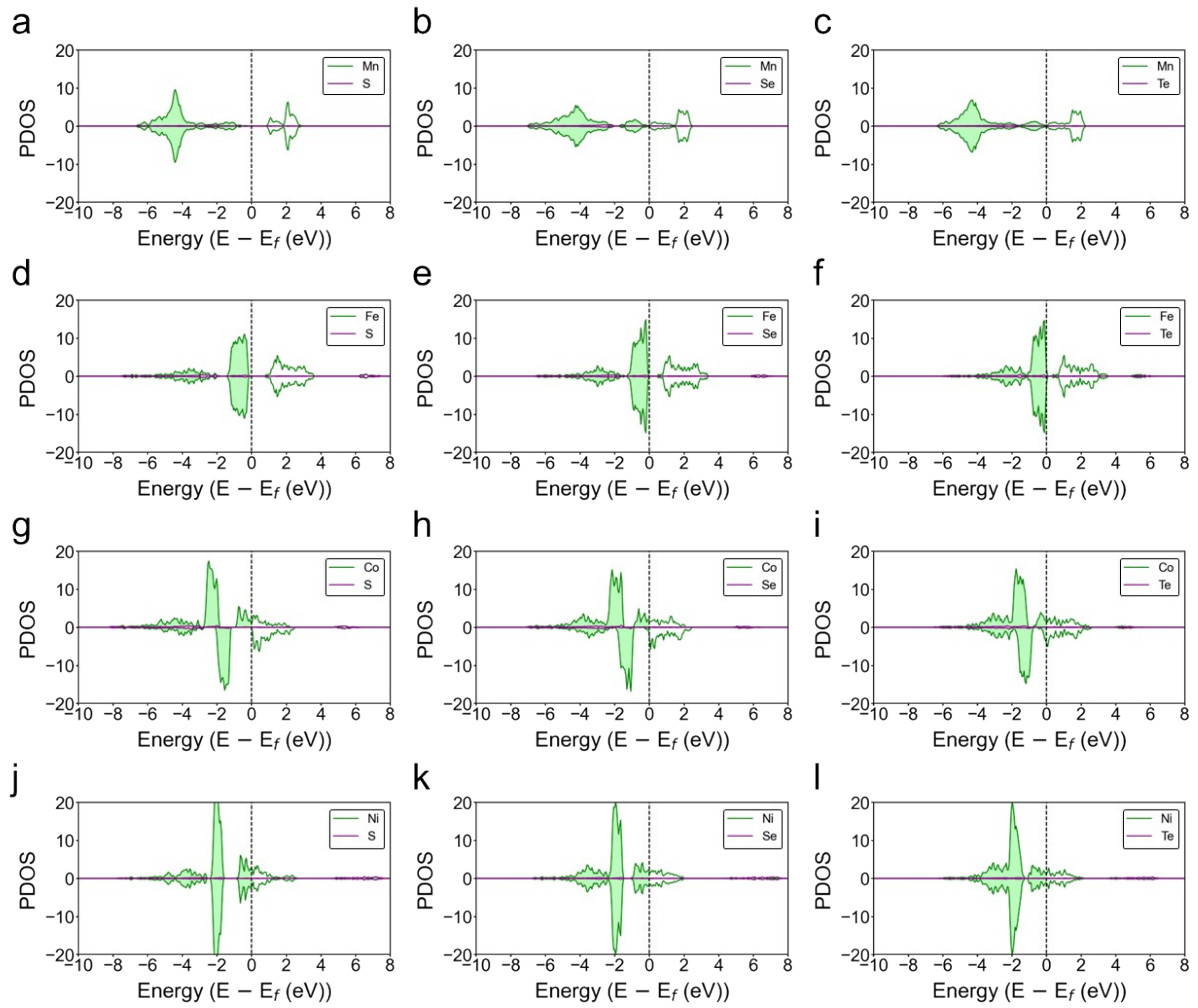
Figure S6. Projected density of states (PDOS) of bulk (a) MnS_2, (b) $MnSe_2$, (c) $MnTe_2$, (d) FeS_2, (e) $FeSe_2$, (f) $FeTe_2$, (g) CoS_2, (h) $CoSe_2$, (i) $CoTe_2$, (j) NiS_2, (k) $NiSe_2$ and (l) $NiTe_2$. Green and purple colors correspond to PDOS of transition metals and chalcogens, respectively. The black dashed line indicates the Fermi energy.
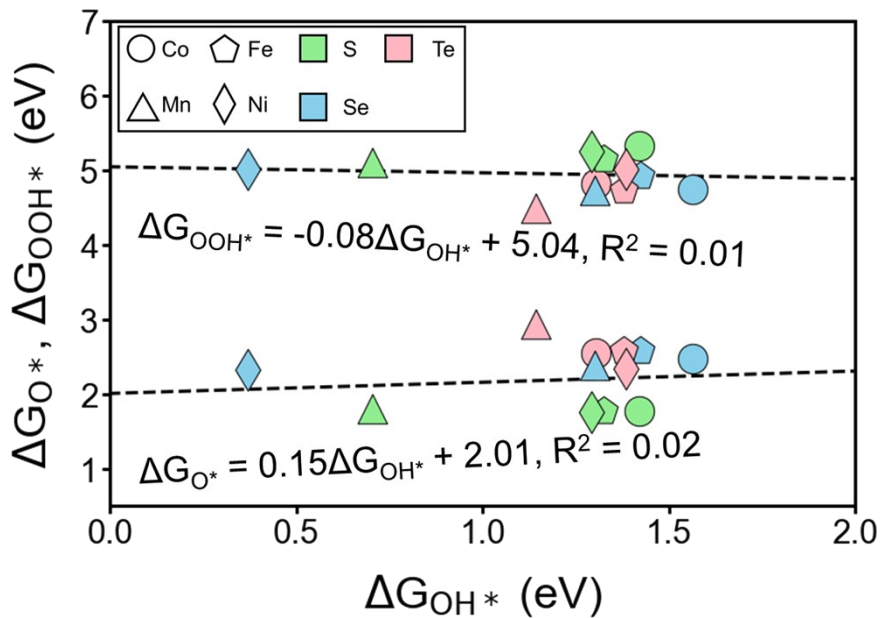
Figure S7. Binding free energies of O* (ΔG_{O*}) and OOH* (ΔG_{OOH*}) plotted with respect to ΔG_{OH*} when chalcogen sites are considered as adsorption sites. No scaling relation was observed. The lower ΔG indicates stronger binding.
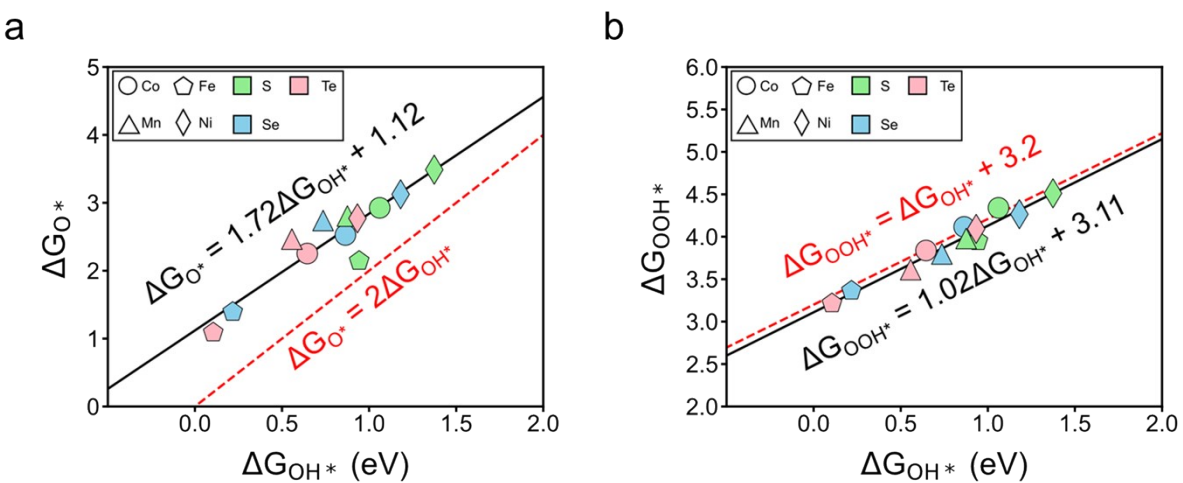
Figure S8. Comparisons of scaling relations for TMD (001) surfaces (black lines) with respect to the conventional scaling relations for transition metals and metal oxides[7] (red dashed lines). (a) ΔG_{O*} vs ΔG_{OH*} and (b) ΔG_{OOH*} vs ΔG_{OH*}.
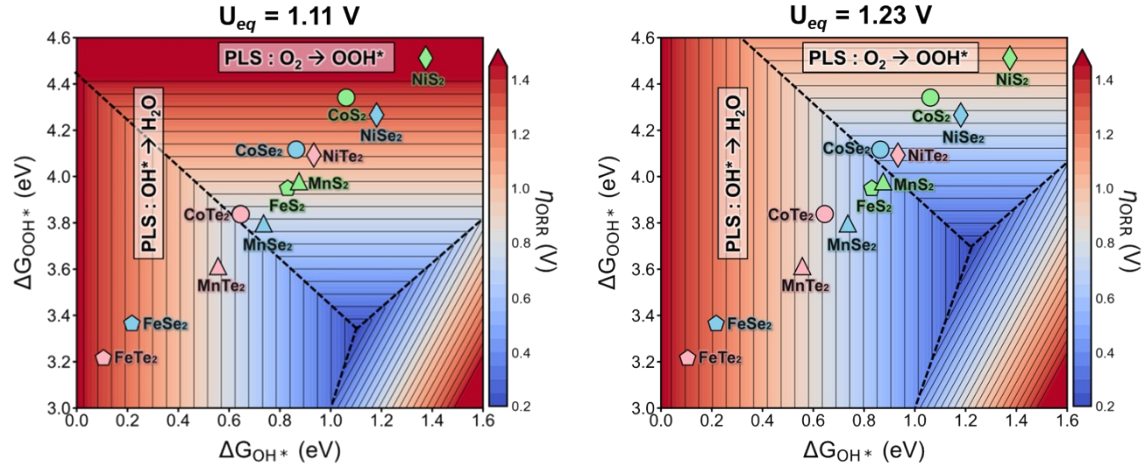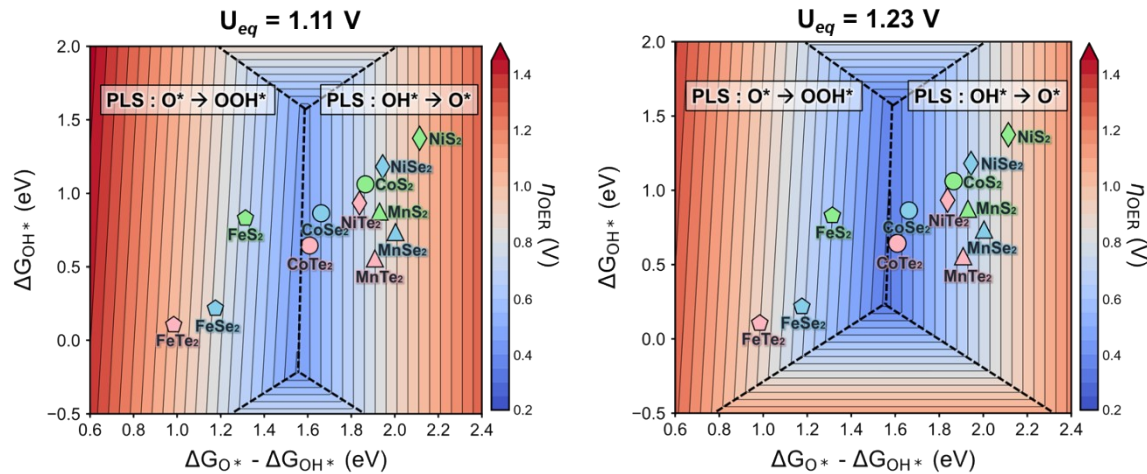
Figure S9. Two-dimensional volcano plots for predicting (a) ORR and (b) OER overpotentials with respect to different equilibrium potential (U_{eq}), 1.11 V of DFT level of theory (left) or 1.23 V of experimental value (right).

Table S1. A summary of DFT calculated and experimentally measured lattice parameters of bulk TMDs. The percentage difference was calculated referenced to the experimental values. PBE+U (U_{eff} = 3 eV) was used only for the relaxation of Mn-based TMDs.

TMDs	DFT calculated lattice parameter (Å)	Experimentally measured lattice parameter (Å)	Difference (%)	Ref
MnS_2	6.18	6.10	1.3	[8]
$MnSe_2$	6.54	6.42	1.9	[9]
$MnTe_2$	7.06	6.94	1.6	[10]
FeS_2	5.41	5.40	0.1	[8]
$FeSe_2$	5.80	5.79	0.3	[11]
$FeTe_2$	6.27	6.29	-0.4	[11]
CoS_2	5.51	5.53	-0.4	[12]
$CoSe_2$	5.85	5.85	0.0	[12]
$CoTe_2$	6.32	6.32	-0.1	[11]
NiS_2	5.60	5.68	-1.4	[8]
$NiSe_2$	5.94	5.96	-0.3	[13]
$NiTe_2$	6.42	6.37	0.8	[11]

Table S2. The ground state DFT energy of TMD bulk systems in antiferromagnetic (AFM) and ferromagnetic (FM) orderings and their differences per formula unit. Energy units are in eV/formula unit.

TMDs	AFM	FM	Energy difference (eV)
MnS_2	-69.18	-68.90	0.07
$MnSe_2$	-63.43	-63.19	0.06
$MnTe_2$	-58.09	-57.85	0.06
FeS_2	-72.12	-72.12	0.00
$FeSe_2$	-64.97	-64.97	0.00
$FeTe_2$	-59.76	-59.76	0.00
CoS_2	-65.51	-65.51	0.00
$CoSe_2$	-59.56	-59.55	0.00
$CoTe_2$	-55.28	-55.28	0.00
NiS_2	-57.90	-57.85	0.01
$NiSe_2$	-52.74	-52.73	0.00
$NiTe_2$	-49.15	-49.14	0.00

Table S3. The ground state magnetic moment per metal atom for bulk structures.

TMDs	Magnetic Moment (μ_B)	Magnetic ordering
MnS_2	4.43	AFM
$MnSe_2$	4.42	AFM
$MnTe_2$	4.39	AFM
FeS_2	0	NM
$FeSe_2$	0	NM
$FeTe_2$	0	NM
CoS_2	0.89	FM
$CoSe_2$	0.78	FM
$CoTe_2$	0.41	FM
NiS_2	0.56	AFM
$NiSe_2$	0.03	AFM
$NiTe_2$	0	NM

Table S4. Summary of U−J values (eV) chosen previously.

TMDs	Functional	U−J values (eV)	Reference
MnS_2	PBE + U	3.9, 2	[14, 15]
$MnSe_2$	PBE + U	-	-
$MnTe_2$	PBE + U	4.2	[16]
FeS_2	PBE + U	2, 1.2, 1.8	[17-19]
$FeSe_2$	PBE + U	3.3	[20]
$FeTe_2$	PBE + U	-	-
CoS_2	PBE + U	4, 2, 5	[21-23]
$CoSe_2$	PBE + U	1, 2, 3	[24-26]
$CoTe_2$	PBE + U	-	-
NiS_2	PBE + U	4.5, 6.39	[27, 28]
$NiSe_2$	PBE + U	4.39, 3.4	[28, 29]
$NiTe_2$	PBE + U	-	-

Table S5. Summary of the previous studies which used PBE functional.

TMDs	Functional	Reference
MnS_2	PBE	[30]
$MnSe_2$	PBE	[31]
$MnTe_2$	PBE	[32]
FeS_2	PBE	[30]
$FeSe_2$	PBE	[33]
$FeTe_2$	PBE	-
CoS_2	PBE	[30, 34-36]
$CoSe_2$	PBE	[31, 37, 38]
$CoTe_2$	PBE	[39]
NiS_2	PBE	[30]
$NiSe_2$	PBE	[31]
$NiTe_2$	PBE	[40]

Table S6. Summary of U_{eff} calculated using linear response approach and the corresponding lattice differences with respect to the experimental values.

TMDs	Linear response $U_{eff}(eV)$	Lattice difference (%)
MnS_2	6.02	1.95
$MnSe_2$	5.92	2.48
$MnTe_2$	5.68	2.52
FeS_2	5.05	3.26
$FeSe_2$	5.00	6.46
$FeTe_2$	4.90	6.28
CoS_2	6.40	4.59
$CoSe_2$	6.46	4.39
$CoTe_2$	6.02	4.86
NiS_2	6.20	2.11
$NiSe_2$	6.34	3.23
$NiTe_2$	6.11	4.14

Table S7. Free energy correction values for gas-phase molecules (H_2 and H_2O) and adsorbates (O*, OH* and OOH*) calculated using the ideal gas and harmonic oscillator approximation, respectively, as implemented in Atomic Simulation Environment (ASE)[41]. Partial pressures of H_2 and H_2O were set to 101,325 and 3,534 Pa, respectively. All values are in eV.

	ZPE	$-TS$	$\int C_p dT$
H_2 (g)	0.26	-0.40	0.09
H_2O (g)	0.57	-0.66	0.11
O*	0.06	-0.07	0.04
OH*	0.34	-0.10	0.06
OOH*	0.41	-0.12	0.06

Table S8. Symbols and definitions of features used in linear regressions.

Elementary atomic properties		Bulk properties	
EN_M	Electronegativity of metal atom	IP_M	Ionization potential of metal atom
EN_C	Electronegativity of chalcogen atom	IP_C	Ionization potential of chalcogen atom
Ea_M	Electron affinity of metal atom	R_M	Covalent radius of metal atom
Ea_C	Electron affinity of chalcogen atom	R_C	Covalent radius of chalcogen atom
$\#3d$	Number of outer d-electrons in the metal atom	q_M	Bader charge of metal atom
$\#3d_U$	Number of unpaired electrons in the metal atom	M-Ch	Metal-Chalcogen bond length

Table S9. Top 10 combinations of features for the linear model sorted by the average value of mean absolute error (MAE) for ΔG_{O*} and ΔG_{OH*} predictions.

Combinations	Average MAE (eV)	Average R^2
$[Ea_M, q_M]$	0.13	0.89
$[\#3d, q_M]$	0.16	0.84
$[Ea_M, R_M]$	0.23	0.67
$[EN_M, \#3d_U]$	0.23	0.67
$[Ea_M, \#3d_U]$	0.23	0.66
$[\#3d, \#3d_U]$	0.23	0.66
$[\#3d, Ea_M]$	0.23	0.66
$[EN_M\ Ea_M]$	0.24	0.65
$[\#3d, R_M]$	0.24	0.65
$[\#3d, EN_M]$	0.24	0.65

Table S10. The binding free energies of O*, OH*, OOH*, the calculated ORR and OER overpotentials and the corresponding potential limiting steps (PLS).

TMDs	Binding Free Energies			ORR		OER	
	$\Delta G(O)$	$\Delta G(OH)$	$\Delta G(OOH)$	η^{ORR}	PLS	η^{OER}	PLS
MnS_2	2.81	0.88	3.98	0.35	OH*→H$_2$O	0.70	OH*→O*
$MnSe_2$	2.74	0.74	3.80	0.49	OH*→H$_2$O	0.77	OH*→O*
$MnTe_2$	2.47	0.56	3.61	0.67	OH*→H$_2$O	0.68	OH*→O*
FeS_2	2.14	0.83	3.95	0.40	OH*→H$_2$O	0.57	O*→OOH*
$FeSe_2$	1.39	0.22	3.36	1.01	OH*→H$_2$O	0.74	O*→OOH*
$FeTe_2$	1.09	0.11	3.22	1.13	OH*→H$_2$O	0.90	O*→OOH*
CoS_2	2.93	1.06	4.34	0.65	O$_2$→OOH*	0.64	OH*→O*
$CoSe_2$	2.53	0.86	4.12	0.43	O$_2$→OOH*	0.43	OH*→O*
$CoTe_2$	2.25	0.65	3.84	0.59	OH*→H$_2$O	0.38	OH*→O*
NiS_2	3.49	1.37	4.51	0.82	O$_2$→OOH*	0.88	OH*→O*
$NiSe_2$	3.13	1.18	4.27	0.58	O$_2$→OOH*	0.71	OH*→O*
$NiTe_2$	2.77	0.93	4.09	0.40	O$_2$→OOH*	0.61	OH*→O*

Table S11. Summary of the calculated ORR and OER overpotentials and the corresponding potential limiting steps (PLS) with respect to different equilibrium potential (U_{eq}) (1.11 V of DFT level of theory and 1.23 V of experimental value).

TMDs	U_{eq} = 1.11 V				U_{eq} = 1.23 V			
	ORR		OER		ORR		OER	
	η^{ORR}	PLS	η^{OER}	PLS	η^{ORR}	PLS	η^{OER}	PLS
MnS$_2$	0.77	O$_2$→OOH*	0.82	OH*→O*	0.35	OH*→H$_2$O	0.70	OH*→O*
MnSe$_2$	0.59	O$_2$→OOH*	0.89	OH*→O*	0.49	OH*→H$_2$O	0.77	OH*→O*
MnTe$_2$	0.67	OH*→H$_2$O	0.80	OH*→O*	0.67	OH*→H$_2$O	0.68	OH*→O*
FeS$_2$	0.62	OH*→H$_2$O	0.69	O*→OOH*	0.40	OH*→H$_2$O	0.57	O*→OOH*
FeSe$_2$	0.89	OH*→H$_2$O	0.86	O*→OOH*	1.01	OH*→H$_2$O	0.74	O*→OOH*
FeTe$_2$	1.01	OH*→H$_2$O	1.02	O*→OOH*	1.13	OH*→H$_2$O	0.90	O*→OOH*
CoS$_2$	1.01	O$_2$→OOH*	0.76	OH*→O*	0.65	O$_2$→OOH*	0.64	OH*→O*
CoSe$_2$	0.79	O$_2$→OOH*	0.55	OH*→O*	0.43	O$_2$→OOH*	0.43	OH*→O*
CoTe$_2$	0.51	OH*→H$_2$O	0.50	OH*→O*	0.59	OH*→H$_2$O	0.38	OH*→O*
NiS$_2$	1.18	O$_2$→OOH*	1.00	OH*→O*	0.82	O$_2$→OOH*	0.88	OH*→O*
NiSe$_2$	0.94	O$_2$→OOH*	0.83	OH*→O*	0.52	O$_2$→OOH*	0.71	OH*→O*
NiTe$_2$	0.76	O$_2$→OOH*	0.73	OH*→O*	0.40	O$_2$→OOH*	0.61	OH*→O*

Table S12. The experimentally measured overpotentials of ORR and OER in an alkaline media.

Materials	η^{ORR} (mV)	η^{OER} (mV)	ref
CoSe$_2$/Se-rGO	327		[5]
Co@DNC@FeS$_2$-0.5	288		[42]
CoO-CoSe$_2$@ N-CNTs/rGO		250	[43]
Co@CoTe$_2$		284	[6]
Fe, Ni-CoS$_2$/GC		242	[44]
NiTe$_2$ nanosheet		310	[45]
FeS$_2$@CoS$_2$		302	[46]
NiSe$_2$/g-C$_3$N$_4$/NF		290	[47]
Fe-CoS$_2$/CoS$_2$@NC		300	[48]
FeSe$_2$@CoSe$_2$/rGO-2		260	[49]

References

1.	Jain, A.; Ong, S. P.; Hautier, G.; Chen, W.; Richards, W. D.; Dacek, S.; Cholia, S.; Gunter, D.; Skinner, D.; Ceder, G., Commentary: The Materials Project: A materials genome approach to accelerating materials innovation. *APL Mater* **2013,** *1* (1), 011002.

2.	Baeumer, C.; Li, J.; Lu, Q.; Liang, A. Y.-L.; Jin, L.; Martins, H. P.; Duchoň, T.; Glöß, M.; Gericke, S. M.; Wohlgemuth, M. A., Tuning electrochemically driven surface transformation in atomically flat LaNiO3 thin films for enhanced water electrolysis. *Nat. Mater.* **2021,** *20* (5), 674-682.

3.	Cococcioni, M.; De Gironcoli, S., Linear response approach to the calculation of the effective interaction parameters in the LDA+ U method. *Phys. Rev. B* **2005,** *71* (3), 035105.

4.	Hammer, B.; Nørskov, J. K., Theoretical surface science and catalysis—calculations and concepts. In *Adv. Catal.*, Elsevier: 2000; Vol. 45, pp 71-129.

5.	Zhao, Y.; Zhang, C.; Fan, R.; Li, J.; Hao, Y.; He, J.; Alonso-Vante, N.; Xue, J., Selenium decorated reduced graphene oxide supported CoSe2 nanoparticles as efficient electrochemical catalyst for the oxygen reduction reaction. *ChemElectroChem* **2018,** *5* (21), 3287-3292.

6.	Qi, Y.; Wu, J.; Xu, J.; Gao, H.; Du, Z.; Liu, B.; Liu, L.; Xiong, D., One-step fabrication of a self-supported Co@ CoTe 2 electrocatalyst for efficient and durable oxygen evolution reactions. *Inorg. Chem. Front.* **2020,** *7* (13), 2523-2532.

7.	Kulkarni, A.; Siahrostami, S.; Patel, A.; Nørskov, J. K., Understanding catalytic activity trends in the oxygen reduction reaction. *Chem. Rev.* **2018,** *118* (5), 2302-2312.

8.	Elliott, N., Interatomic distances in FeS2, CoS2, and NiS2. *J. Chem. Phys.* **1960,** *33* (3), 903-905.

9.	Liu, X.; Ma, J.; Peng, P.; Zheng, W., Hydrothermal synthesis of cubic MnSe2 and octahedral α-MnSe microcrystals. *J. Cryst. Growth* **2009,** *311* (5), 1359-1363.

10.	Hastings, J.; Elliott, N.; Corliss, L., Antiferromagnetic Structures of Mn S 2, Mn Se 2, and Mn Te 2. *Phys. Rev.* **1959,** *115* (1), 13.

11.	Bither, T. A.; Bouchard, R.; Cloud, W.; Donohue, P.; Siemons, W., Transition metal pyrite dichalcogenides. High-pressure synthesis and correlation of properties. *Inorg. Chem.* **1968,** *7* (11), 2208-2220.

12.	Kong, D.; Cha, J. J.; Wang, H.; Lee, H. R.; Cui, Y., First-row transition metal dichalcogenide catalysts for hydrogen evolution reaction. *Energy Environ. Sci.* **2013,** *6* (12), 3553-3558.

13.	Wang, S.; Li, W.; Xin, L.; Wu, M.; Long, Y.; Huang, H.; Lou, X., Facile synthesis of truncated cube-like NiSe2 single crystals for high-performance asymmetric supercapacitors. *Chem. Eng. J.* **2017,** *330*, 1334-1341.

14.	Durkee, D.; Smith, D.; Torchio, R.; Petitgirard, S.; Briggs, R.; Kantor, I.; Evans, S. R.; Chatterji, T.; Irifune, T.; Pascarelli, S., Electronic origins of the giant volume collapse in the pyrite mineral MnS2. *J. Solid State Chem.* **2019,** *269*, 540-546.

15.	Kimber, S. A.; Salamat, A.; Evans, S. R.; Jeschke, H. O.; Muthukumar, K.; Tomić, M.; Salvat-Pujol, F.; Valentí, R.; Kaisheva, M. V.; Zizak, I., Giant pressure-induced volume collapse in the pyrite mineral MnS2. *Proc. Natl. Acad. Sci. U.S.A.* **2014,** *111* (14), 5106-5110.

16.	Ma, H.; Yang, H.; Zhang, X.; Duan, B.; Li, W.; Zhai, P.; Li, G., First-principle predictions of the electric and thermal transport performance on high-temperature thermoelectric semiconductor MnTe2. *J. Alloys Compd* **2022,** *898*, 162813.

17.	Wen, X.; Liang, Y.; Bai, P.; Luo, B.; Fang, T.; Yue, L.; An, T.; Song, W.; Zheng, S., First-principles calculations of the structural, elastic and thermodynamic properties of mackinawite (FeS) and pyrite (FeS2). *Phys. B: Condens. Matter* **2017,** *525*, 119-126.

18.   Xi, P.; Shi, C.; Yan, P.; Liu, W.; Tang, L., DFT study on the influence of sulfur on the hydrophobicity of pyrite surfaces in the process of oxidation. *Appl. Surf. Sci.* **2019,** *466*, 964-969.

19.   Ray, D.; Voigt, B.; Manno, M.; Leighton, C.; Aydil, E. S.; Gagliardi, L., Sulfur vacancy clustering and its impact on electronic properties in pyrite FeS_2. *Chem. Mater* **2020,** *32* (11), 4820-4831.

20.   Li, G.; Zhang, B.; Rao, J.; Herranz Gonzalez, D.; Blake, G. R.; de Groot, R. A.; Palstra, T. T., Effect of vacancies on magnetism, electrical transport, and thermoelectric performance of marcasite $FeSe_2 - \delta$ ($\delta = 0.05$). *Chem. Mater* **2015,** *27* (24), 8220-8229.

21.   Liu, W.; Hu, E.; Jiang, H.; Xiang, Y.; Weng, Z.; Li, M.; Fan, Q.; Yu, X.; Altman, E. I.; Wang, H., A highly active and stable hydrogen evolution catalyst based on pyrite-structured cobalt phosphosulfide. *Nat. Commun.* **2016,** *7* (1), 1-9.

22.   Feng, Z.-Y.; Yang, Y.; Zhang, J.-M., First-principles study of the structural and electronic properties of $CoX0.25S1.75$ (X= F, Cl, or Br). *J. Phys. Chem. Solids* **2018,** *123*, 284-293.

23.   Day-Roberts, E.; Birol, T.; Fernandes, R. M., Contrasting ferromagnetism in pyrite FeS_2 induced by chemical doping versus electrostatic gating. *Phys. Rev. Mater.* **2020,** *4* (5), 054405.

24.   Liu, Y.; Hua, X.; Xiao, C.; Zhou, T.; Huang, P.; Guo, Z.; Pan, B.; Xie, Y., Heterogeneous spin states in ultrathin nanosheets induce subtle lattice distortion to trigger efficient hydrogen evolution. *J. Am. Chem. Soc.* **2016,** *138* (15), 5087-5092.

25.   Liu, Y.; Cheng, H.; Lyu, M.; Fan, S.; Liu, Q.; Zhang, W.; Zhi, Y.; Wang, C.; Xiao, C.; Wei, S., Low overpotential in vacancy-rich ultrathin $CoSe_2$ nanosheets for water oxidation. *J. Am. Chem. Soc* **2014,** *136* (44), 15670-15675.

26.   Sun, Y.; Li, X.; Zhang, T.; Xu, K.; Yang, Y.; Chen, G.; Li, C.; Xie, Y., Nitrogen-Doped Cobalt Diselenide with Cubic Phase Maintained for Enhanced Alkaline Hydrogen Evolution. *Angew. Chem.* **2021,** *133* (39), 21745-21752.

27.   Liu, H.; He, Q.; Jiang, H.; Lin, Y.; Zhang, Y.; Habib, M.; Chen, S.; Song, L., Electronic structure reconfiguration toward pyrite NiS_2 via engineered heteroatom defect boosting overall water splitting. *ACS nano* **2017,** *11* (11), 11574-11583.

28.   Schuster, C.; Gatti, M.; Rubio, A., Electronic and magnetic properties of NiS_2, NiSSe and $NiSe_2$ by a combination of theoretical methods. *Eur Phys J B* **2012,** *85* (9), 1-10.

29.   Zuo, Y.; Rao, D.; Ma, S.; Li, T.; Tsang, Y. H.; Kment, S.; Chai, Y., Valence engineering via dual-cation and boron doping in pyrite selenide for highly efficient oxygen evolution. *ACS nano* **2019,** *13* (10), 11469-11476.

30.   Wu, M.-H.; Chou, W.-J.; Huang, J.-S.; Putungan, D. B.; Lin, S.-H., First-principles investigation of the hydrogen evolution reaction on different surfaces of pyrites MnS_2, FeS_2, CoS_2, NiS_2. *Phys. Chem. Chem. Phys.* **2019,** *21* (38), 21561-21567.

31.   Pathak, M.; Tamang, D.; Kandasamy, M.; Chakraborty, B.; Rout, C. S., A comparative experimental and theoretical investigation on energy storage performance of $CoSe_2$, $NiSe_2$ and $MnSe_2$ nanostructures. *Appl. Mater. Today* **2020,** *19*, 100568.

32.   Thapa, B.; Patra, P.; Subba, N.; Shankar, A., Effect of Mn doping in mechanical properties of $Cd1 - xMnxTe_2$. *Mater. Res. Express* **2019,** *6* (11), 116322.

33.   Ghosh, A.; Thangavel, R., Electronic structure and optical properties of iron based chalcogenide FeX_2 (X= S, Se, Te) for photovoltaic applications: a first principle study. *Indian J. Phys.* **2017,** *91* (11), 1339-1344.

34.   Cabán-Acevedo, M.; Stone, M. L.; Schmidt, J.; Thomas, J. G.; Ding, Q.; Chang, H.-C.; Tsai, M.-L.; He, J.-H.; Jin, S., Efficient hydrogen evolution catalysis using ternary pyrite-type cobalt phosphosulphide. *Nat. Mater.* **2015,** *14* (12), 1245-1251.

35. Sheng, H.; Hermes, E. D.; Yang, X.; Ying, D.; Janes, A. N.; Li, W.; Schmidt, J.; Jin, S., Electrocatalytic production of H2O2 by selective oxygen reduction using earth-abundant cobalt pyrite (CoS2). *ACS Catal.* **2019,** *9* (9), 8433-8442.

36. Zhang, J.; Xiao, B.; Liu, X.; Liu, P.; Xi, P.; Xiao, W.; Ding, J.; Gao, D.; Xue, D., Copper dopants improved the hydrogen evolution activity of earth-abundant cobalt pyrite catalysts by activating the electrocatalytically inert sulfur sites. *J. Mater. Chem. A* **2017,** *5* (33), 17601-17608.

37. Liu, Y.; Chen, Z.; Jia, H.; Xu, H.; Liu, M.; Wu, R., Iron-doping-induced phase transformation in dual-carbon-confined cobalt diselenide enabling superior lithium storage. *ACS nano* **2019,** *13* (5), 6113-6124.

38. Zhang, X.-L.; Hu, S.-J.; Zheng, Y.-R.; Wu, R.; Gao, F.-Y.; Yang, P.-P.; Niu, Z.-Z.; Gu, C.; Yu, X.; Zheng, X.-S., Polymorphic cobalt diselenide as extremely stable electrocatalyst in acidic media via a phase-mixing strategy. *Nat. Commun.* **2019,** *10* (1), 1-9.

39. Zheng, Y.-R.; Wu, P.; Gao, M.-R.; Zhang, X.-L.; Gao, F.-Y.; Ju, H.-X.; Wu, R.; Gao, Q.; You, R.; Huang, W.-X., Doping-induced structural phase transition in cobalt diselenide enables enhanced hydrogen evolution catalysis. *Nat. Commun.* **2018,** *9* (1), 1-9.

40. Zhang, J.-F.; Zhao, Y.; Liu, K.; Liu, Y.; Lu, Z.-Y., First-principles study of the crystal structure, electronic structure, and transport properties of NiTe 2 under pressure. *Phys. Rev. B.* **2021,** *104* (3), 035111.

41. Larsen, A. H.; Mortensen, J. J.; Blomqvist, J.; Castelli, I. E.; Christensen, R.; Dułak, M.; Friis, J.; Groves, M. N.; Hammer, B.; Hargus, C., The atomic simulation environment—a Python library for working with atoms. *Journal of Physics: Condensed Matter* **2017,** *29* (27), 273002.

42. Liu, M.; Zhang, M.; Zhang, P.; Xing, Z.; Jiang, B.; Yu, Y.; Cai, Z.; Li, J.; Zou, J., ZIF-67-derived dodecahedral Co@ N-doped graphitized carbon protected by a porous FeS2 thin-layer as an efficient catalyst to promote the oxygen reduction reaction. *ACS Sustain. Chem. Eng.* **2020,** *8* (10), 4194-4206.

43. Xu, D.; Long, X.; Xiao, J.; Zhang, Z.; Liu, G.; Tong, H.; Liu, Z.; Li, N.; Qian, D.; Li, J., Rationally constructing CoO and CoSe2 hybrid with CNTs-graphene for impressively enhanced oxygen evolution and DFT calculations. *Chem. Eng. J.* **2021,** *422*, 129982.

44. Peng, W.; Deshmukh, A.; Chen, N.; Lv, Z.; Zhao, S.; Li, J.; Yan, B.; Gao, X.; Shang, L.; Gong, Y., Deciphering the Dynamic Structure Evolution of Fe-and Ni-Codoped CoS2 for Enhanced Water Oxidation. *ACS Catal.* **2022,** *12*, 3743-3751.

45. Yang, L.; Xu, H.; Liu, H.; Cheng, D.; Cao, D., Active site identification and evaluation criteria of in situ grown CoTe and NiTe nanoarrays for hydrogen evolution and oxygen evolution reactions. *Small Methods* **2019,** *3* (5), 1900113.

46. Li, Y.; Yin, J.; An, L.; Lu, M.; Sun, K.; Zhao, Y. Q.; Gao, D.; Cheng, F.; Xi, P., FeS2/CoS2 interface nanosheets as efficient bifunctional electrocatalyst for overall water splitting. *Small* **2018,** *14* (26), 1801070.

47. Wang, S.; He, P.; Jia, L.; He, M.; Zhang, T.; Dong, F.; Liu, M.; Liu, H.; Zhang, Y.; Li, C., Nanocoral-like composite of nickel selenide nanoparticles anchored on two-dimensional multi-layered graphitic carbon nitride: a highly efficient electrocatalyst for oxygen evolution reaction. *Appl. Catal. B* **2019,** *243*, 463-469.

48. Yang, C.; Chang, Y.-X.; Kang, H.; Li, Y.; Yan, M.; Xu, S., Fe-doped CoS2 nanoparticles supported CoS2 microspheres@ N-doped carbon electrocatalyst for enhanced oxygen evolution reaction. *Appl. Phys. A* **2021,** *127* (6), 1-9.

49. Zhu, G.; Xie, X.; Li, X.; Liu, Y.; Shen, X.; Xu, K.; Chen, S., Nanocomposites based on CoSe2-decorated FeSe2 nanoparticles supported on reduced graphene oxide as

high-performance electrocatalysts toward oxygen evolution reaction. *ACS Appl. Mater. Interfaces* **2018,** *10* (22), 19258-19270.